



Regulation of epithelial tissue homeostasis by active transepithelial transport

Huiqiong Wu^a, Charlie Duclut^{b,1} , Gregory Arkowitz^a , Ranjith Chilupuri^a , Tien Dang^a, Jacques Prost^b , Benoit Ladoux^{a,c,d,1} , and René-Marc Mège^{a,1}

Affiliations are included on p. 10.

Edited by Marianne Bronner, California Institute of Technology, Pasadena, CA; received February 13, 2025; accepted October 2, 2025

Epithelia are intricate tissues whose function is intimately linked to mechanics. While mechanobiology has primarily focused on factors such as cell-generated contractility and mechanical properties of extracellular matrix, an interesting mechanobiological paradigm highlights the role of osmotic and mechanical pressures in shaping epithelial tissues. In our study, we developed an *in vitro* model of cell-coated microsized hydrogel spheres (MHSs) which allows to decipher the interplay between cellular activities and tissue mechanics. Drastic, isotropic MHS compressions were observed once the epithelia reached confluence. Further studies revealed that the compression was a process independent of cell contractility but rather regulated by active transepithelial fluid flow. Compressive stresses of about 7 kPa are generated by such an active hydraulic mechanism. Tissue homeostasis is then maintained by a fine balance between cell proliferation and extrusion. Our findings demonstrate the critical role of fluid transport in generating mechanical forces within epithelial tissues. Supported by a theoretical mechanohydraulic model, a mechanistic framework for understanding the intricate interplay between cellular processes and tissue mechanics was established. These results challenge traditional views of epithelial tissue mechanics, emphasizing the pivotal influence of osmotic and mechanical pressures in shaping tissues. We anticipate that this study will advance the understanding of epithelial tissue development, the maintenance of homeostasis, and the mechanisms underlying pathological conditions.

tissue mechanics | epithelial homeostasis | tissue hydraulics | active transport | osmotic pressure

Epithelial tissues serve as the protective linings of organs, creating vital barriers and functional interfaces between internal and external environments. Dysfunctions within epithelial layers lead to severe organ failures, making the understanding of their development and maintenance critically important. Apart from biochemical signaling, abundant literature points out the importance of mechanics on epithelial morphogenesis and homeostasis (1, 2). Physical properties of extracellular matrix (ECM) and neighboring tissues have been shown to regulate collective cell migration (3–5), tissue organization, epithelia folding (4–6), and integrity (7, 8).

Cells as active systems generate and adapt internal stresses and traction forces (9) in response to these mechanical cues. The underlying mechanisms rely on actomyosin-generated forces (1, 2, 10, 11), as well as cell–matrix and cell–cell adhesions mechanotransduction and -sensing (12–14). However, cell contractility fails to explain some tissue behaviors highlighting alternative mechanisms, such as active ion and water transport through which cells can generate stresses (15–19). Despite the existence of fluid and osmolyte gradients in organs and tissues, including epithelia, the role of active ionic transport and water flow has been largely overlooked to understand epithelial cell behavior.

Fluid transport and mechanical pressure have been shown to be crucial for organ shaping including the lung, kidney, vasculature, and mammary glands (17, 20, 21). During murine lung development, the transmural pressure created by active fluid secretion of epithelial cells controls the airway branching (17). In regenerating *Hydra* spheroid, the inflation driven by transepithelial pumping creates mechanical stimuli that activate the Wnt3 signaling of head organizers (18). In the nematode germline, hydraulic instabilities among germ cells determine the cell fate (22). In developmental processes, such as inner ear and larva-polyp morphogenesis, epithelial tissues deposit highly charged ECM which creates osmotic pressures, thereby promoting tissue morphogenesis (23, 24). Transepithelial fluid transport, generating hydraulic pressure within the inner cell mass, is a prerequisite for mammalian embryonic development (19, 25). Stress balance between the mechanical pressure in the lumen and tissue tension results in cyclic inflation–deflations, thereby regulating tissue and organ size (26, 27).

Significance

Epithelial tissues are central to organ function, yet the physical mechanisms governing their mechanics are still being uncovered. Here, we reveal that epithelial cells can generate substantial compressive stresses—approximately 7 kPa—not through contractile forces, but via active transepithelial ion and fluid transport. Using a model of microsized hydrogel spheres coated with epithelial cells, we show that this active hydraulic mechanism drives isotropic tissue compression and maintains homeostasis through a balance of cell proliferation and extrusion. Supported by a theoretical mechanohydraulic model, these findings challenge contractility-centered paradigms and establish osmotic pressure as fundamental determinants of epithelial architecture. This framework provides insight into tissue morphogenesis, stability, and disease-related mechanical dysfunction.

The authors declare no competing interest.

This article is a PNAS Direct Submission.

Copyright © 2025 the Author(s). Published by PNAS. This article is distributed under Creative Commons Attribution-NonCommercial-NoDerivatives License 4.0 (CC BY-NC-ND).

¹To whom correspondence may be addressed. Email: charlie.duclut@curie.fr, benoit.ladoux@fau.de, or rene-marc.mège@ijm.fr.

This article contains supporting information online at <https://www.pnas.org/lookup/suppl/doi:10.1073/pnas.2503156122/-DCSupplemental>.

Published November 11, 2025.

Epithelial cell lines are classical *in vitro* models to study fluid transport and lumen formation. In particular, Madin-Darby Canine Kidney (MDCK) cells are apicobasal polarized and behave as semipermeable membranes (28, 29). Their efficiency for fluid transport depends on a high transepithelial resistance, regulated by tight junctions, enabling the formation of transepithelial osmotic gradients (30, 31). In 3-dimensional (3D) environments, MDCK cells self-organize into cysts with polarities dependent on culture conditions, i.e., when cultured in ECM gels, their apical side faces the lumen while in suspensions their basal side faces the lumen (32). Regardless of the polarity orientation, the lumen expansion relies on water influx that arises from ion and hydrostatic pressure gradients (33, 34). When cultured on impermeable two-dimensional (2D) surfaces, MDCK cells form blisters or domes that result from cellular detachment from the underlying surface (35, 36). The formation of these blisters is caused by an increase of the basal hydrostatic pressure established by apical-to-basal fluid flux. This basal hydrostatic pressure nucleates local intercellular fractures, thus promoting the assembly of suspended multicellular structures that can sustain large deformations (37).

To further investigate the mechanical constraints imposed by both cellular contractility and hydraulic stresses on 3D epithelial tissues, we developed a synthetic model of 3D MDCK epithelial layers covering biofunctionalized Micro-sized Hydrogel Spheres (MHSs). We show that at confluence, epithelial cells actively deform the MHSs not through cellular contractility but rather through active pumping, leading to the build-up of an osmotic pressure difference that drives the deflation of the MHS. This

compression relies on the establishment of an appropriate barrier function as well as ion and water transport across the epithelial tissue. After compression, the epithelium adapts to the reduced surface area not only by altering cell shape but also by maintaining a balance between cell division and extrusion as described in 2D cell cultures (38, 39). Our experimental results are supported by a theoretical model that incorporates both tissue tension and fluid transport. This model provides insights into the mechanisms underlying both the maintenance of the homeostatic state and the observed fluctuations around it. Together, our results highlight the significant role of fluid transport in epithelial mechanics and consequent tissue homeostasis regulation.

Results

3D Epithelial Monolayers Compress MHSs via Stresses Independent of Cell Contractility. We first prepared fibronectin-functionalized polyethylene glycol diacrylate (PEGDA) MHSs by a simple emulsion synthesis (*Materials and Methods*). These MHSs were then sowed with epithelial cells and embedded in agarose to allow for live imaging (*SI Appendix*, Fig. S1). Epithelial cells, initially sparsely distributed, spread well and proliferate on the MHSs up to confluence (Fig. 1A and Movie S1). We observed that the MHSs systematically underwent substantial isotropic compression that only started after cells reached confluence (Fig. 1B). Quantitative analysis demonstrated a consistent maximum reduction in MHS diameter of $21 \pm 3\%$ for MDCK cells and $23 \pm 3\%$ for human colorectal adenocarcinoma (Caco-2) cells (Fig. 1 C, D, and F and Movie S2), irrespective of the initial size. These

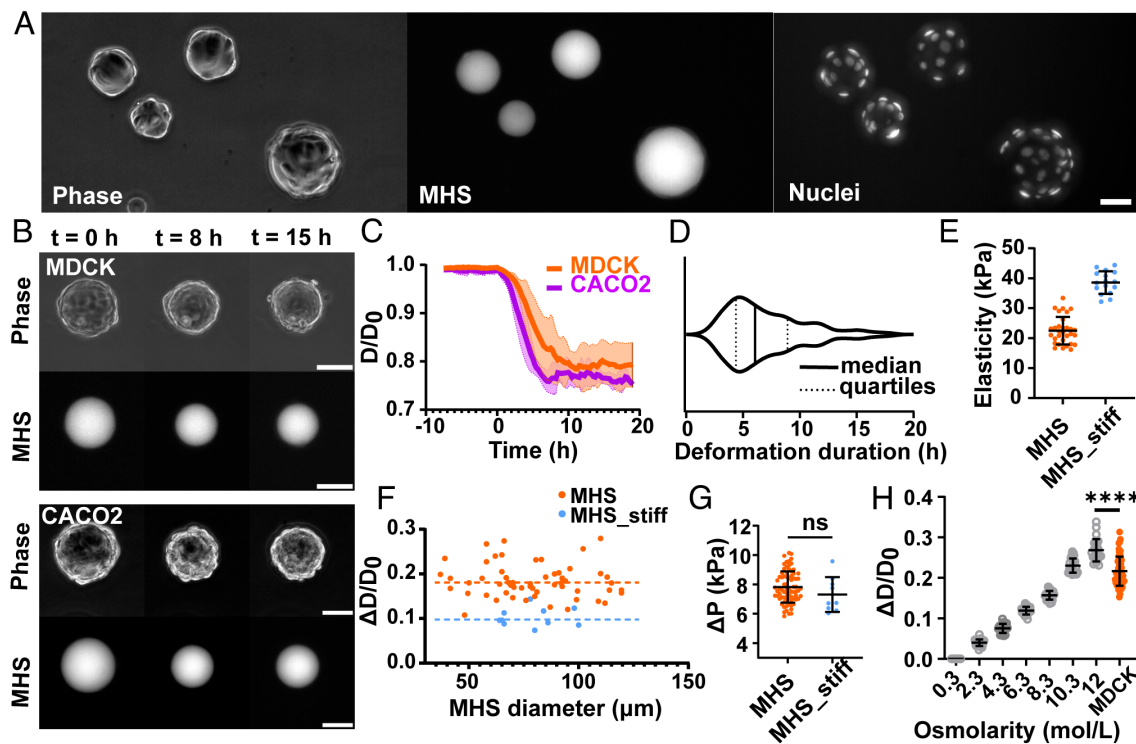


Fig. 1. MHS deformation mediated by epithelial tissues. MDCK (A) and Caco-2 (B) epithelial cells cultured on MHSs. Phase image (Left), MHS channel (Middle), and Nuclei channel (Right); (Scale bar: 50 μ m.) (C) Averaged evolution curves of the MHS diameters when cultured with MDCK (Orange, n = 12, N = 3) or Caco-2 cells (purple, n = 6, N = 1). Time is normalized to the onset of MHS size reduction. (D) Violin plots of deformation duration distribution with MDCK epithelia, n = 123, N = 4. (E) Indentation measurement results of the Young's modulus of two different MHS compositions, MHS used throughout the study when not specified (n = 31, N = 3), MHS_Stiff (n = 16, N = 3). (F) MHS deformations as a function of initial MHS sizes; orange dots represent MHSs with lower rigidity (n = 82, N = 3) and blue dots represent MHS_stiff (n = 9, N = 1); The straight dotted-lines are the mean values, respectively. (G) Compressive stresses inferred from MHS deformations, n (MHS) = 58, N = 3; n (MHS_stiff) = 10; N = 1. (H) Deformations of bare MHS in deswelling experiments. Varied osmolarities were obtained by adding extra NaCl to the culture media; (MDCK): MHSs seeded with epithelial cells in media with physiological osmolarity (0.3 mol/L). n = 24, N = 4 for each condition without cells; n = 56, N = 3 for deformation with MDCK cells. ns: t test results, P > 0.05; ****: t test results, P ≤ 0.0001.

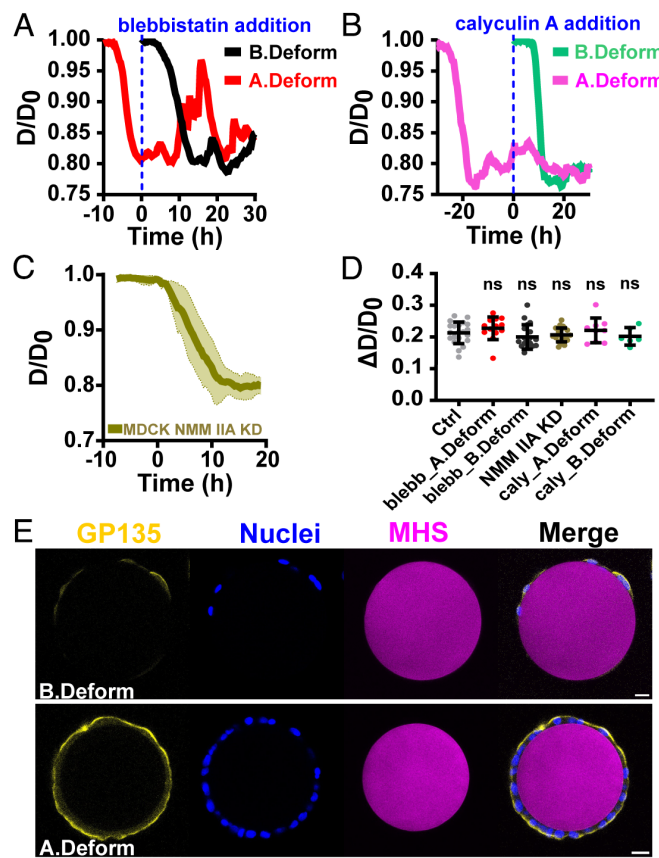


Fig. 2. Tissue contractility modulation. (A) Representative size evolution curves of MHSs under blebbistatin treatment ($20 \mu\text{M}$), drug was administered at $t = 0$ h. (B) Representative size evolution curves of MHSs under calyculin A treatment (5nM), drug was administered at $t = 0$ h. (C) Averaged size evolution curves of MHSs seeded with MDCK NMM IIA KD cells, here time is normalized to the start of each deformation, $N = 2$, $n = 9$. (D) Quantification of deformations under different contractility modulation conditions, (A.Deform) $n = 13$, $N = 3$; (B.Deform) $n = 19$, $N = 3$; (NMM IIA KD) $n = 23$, $N = 2$; (caly.A.Deform) $n = 9$, $N = 1$; (B.Deform) $n = 6$, $N = 1$. B.Deform and A.deform stands for administration before and after deformation respectively. (E) Immunostaining of apical marker GP135, before deformation (B.Deform) and after deformation (A.Deform). (Scale bars, $20 \mu\text{m}$.)

reductions correspond to volume decreases of 51% and 68%, respectively. Although the precise moment when cells reached confluence on each MHS could not be determined, the duration of compression—defined as the time from the onset of deformation to when the MHSs reached their minimum diameters—was approximately 6 h. By 10 h, ~83% of the maximum deformation had been achieved (Fig. 1D).

We then calculated the amount of stress developed by the tissue to compress the MHSs. We determined the Young's modulus of the MHSs to be $22.5 \pm 4.4 \text{ kPa}$ using nano-indentation (Fig. 1E). Knowing the elastic modulus, we inferred from the observed maximal compression the compressive stress to be $7.8 \pm 1 \text{ kPa}$ (Fig. 1G). To investigate whether this mechanical deformation was dependent on hydrogel stiffness, we prepared stiffer MHSs—stiff (Young modulus = $38.6 \pm 3.6 \text{ kPa}$) (Fig. 1E). When MDCK cells reached confluence on these stiffer substrates, we observed a maximum reduction in MHS diameter of $10 \pm 2\%$ regardless of the initial MHS size (Fig. 1F), corresponding to a tissue-generated compressive stress of $7.3 \pm 1 \text{ kPa}$ (Fig. 1G). These results show that tissue-generated stresses are independent of substrate stiffness. Overall, our findings suggest that the stress driving MHS deformation may be independent of cell contractile-based forces, which have been reported to be rigidity-dependent at the single cell

(40–42) and collective cell levels (3, 14). Next, we explored whether the final compression state of MHSs was determined by the material properties of the hydrogel or governed by the epithelial tissue covering it. Simple deswelling experiments (43) revealed a progressive reduction in MHS diameters when naked MHSs were incubated in media with increasing NaCl concentrations (Fig. 1H). Notably, to obtain significant radius reductions, as those observed in the presence of an epithelium, one needs to reach extremely high osmolarities, typically 10 mol/L ruling out a direct effect of deswelling on the hydrogel.

Next, we delved into understanding the underlying source of the stress responsible for the deformation of the MHSs. To further investigate the role of actomyosin-based contractility, we inhibited nonmuscle myosin II (NMM II) activity using blebbistatin, applied either before or after compression. This treatment had no significant effect on the maximal compression achieved (Fig. 2 A and D). Similarly, treatment with calyculin A, a phosphatase inhibitor that enhances cellular contractility, did not affect MHS compression (Fig. 2 B and D). These findings reinforce the hypothesis that acto-myosin contractility is not the driving stress behind MHS deformation. Finally, we observed that MDCK cells knockdown for NMM IIA (NMM IIA KD) (44) compressed the MHSs as efficiently as WT cells (Fig. 2 C and D). Altogether, these results demonstrate that the MHS compression could not result from contractile forces generated by the actomyosin cytoskeleton.

Proper Barrier Function, Osmotic Gradient, and Water Outflow Are Required for MHS Compression. To induce compression of the MHSs, regardless of the source of the mechanical stress involved, the incompressible fluid must be expelled from the MHSs. High-resolution confocal live imaging of MDCK LifeAct-GFP (SI Appendix, Fig. S2) revealed that MHS compression coincides with a reduction in MHS-tissue total volume, indicative of a transepithelial fluid outflow (Fig. 3A). MDCK cells possess active transepithelial ion transport abilities (28, 29, 36). From MHS compression rate, we estimated an average water efflux rate per unit area of $0.27 \pm 0.13 \text{ } \mu\text{L} \cdot \text{h}^{-1} \cdot \text{cm}^{-2}$, consistent with previously reported flux rates for MDCK cysts in 3D cultures [$0.25 \pm 0.03 \text{ } \mu\text{L} \cdot \text{h}^{-1} \cdot \text{cm}^{-2}$ (45), $0.22 \pm 0.01 \text{ } \mu\text{L} \cdot \text{h}^{-1} \cdot \text{cm}^{-2}$ (46)]. Reported flux rates for 2D MDCK monolayers vary widely from 0 to $10 \text{ } \mu\text{L} \cdot \text{h}^{-1} \cdot \text{cm}^{-2}$ (47), depending on culture conditions and measurement methods, although higher values can be obtained in a apical–basal zero-pressure difference condition (48). We therefore hypothesized that active electrolytes transport across the cell monolayer establishes a transepithelial osmotic gradient, resulting in subsequent water outflow leading to MHS compression. If MHS compression is due to transepithelial outflow governed by osmotic gradients, the maximal compression of MHSs should change upon sudden changes in external osmolarity. When applying a series of hypotonic and hypertonic shocks, we indeed observed significant changes in MHS compression (Fig. 3B and SI Appendix, Fig. S3). Hypertonic shocks at 0.45 and 0.4 mol/L caused further MHS compression compared to physiological osmolarity (0.3 mol/L). Conversely, hypotonic shocks led to MHS relaxations, decreasing the equilibrium MHS compression to $19.0 \pm 3.1\%$, $13.6 \pm 2.1\%$, and $11.7 \pm 1.3\%$ for 0.2 , 0.15 , and 0.1 mol/L , respectively.

To establish a transepithelial osmotic gradient, cells first need to acquire polarized transport ability which is linked to their apical–basal polarity (Fig. 3A). Immunostaining for the apical marker podocalyxin (GP135) (49) revealed that the cells were polarized, with the GP135-positive apical side oriented toward the culture medium, even before the onset of MHS compression (Fig. 2E). Nonconfluent MDCK cells do not have the ability to build transepithelial osmotic gradients due to paracellular free diffusion. For

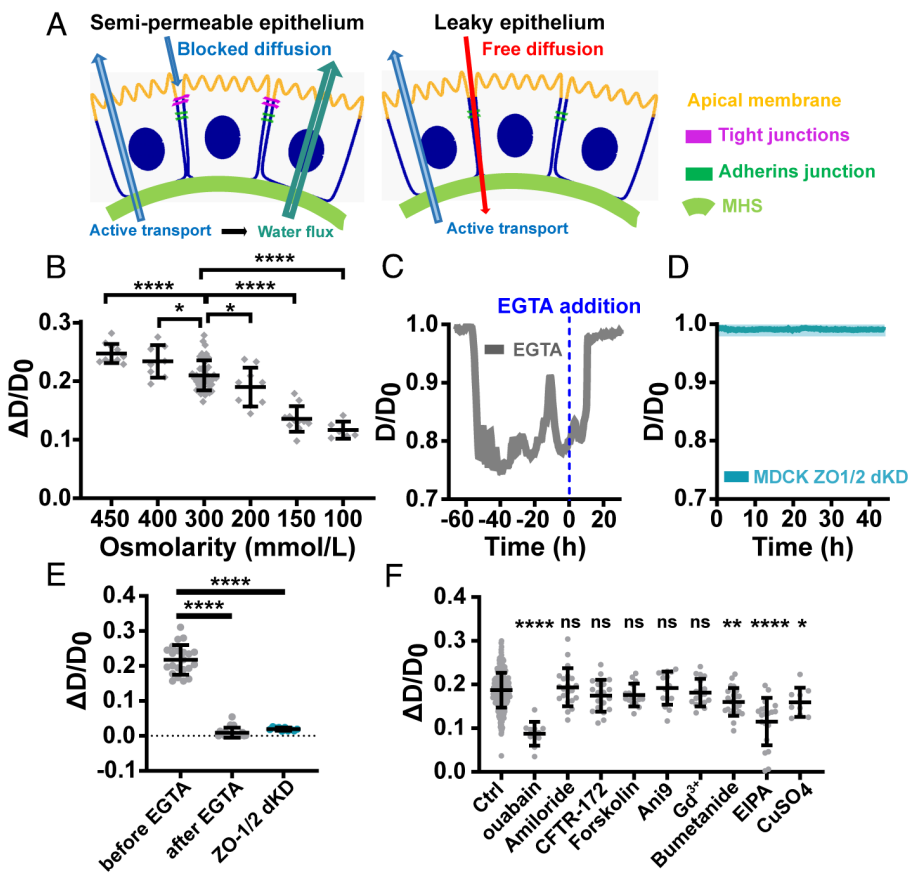


Fig. 3. Tissue barrier function and active transport in regulating MHS deformations. (A) Schematics of semipermeable and leaky epithelia and corresponding substance transports. (B) Quantification of deformations under different osmotic shock conditions. n (0.45 mol/L) = 11, N = 1; n (0.4 mol/L) = 8, N = 1; n (0.3 mol/L) = 45, N = 3; n (0.2 mol/L) = 9, N = 1; n (0.15 mol/L) = 11, N = 1; n (0.1 mol/L) = 6, N = 1. (C) Representative diameter evolution curve of MHS when treated by Ethylene Glycol-tetraacetic acidVAD-FMK — Valine-Alanine-Aspartic acid-Fluoromethyl Ketone (EGTA) (3 mM). (D) Averaging diameter evolution curves over time of MHSs seeded with MDCK ZO-1/2 dKD cells. n = 10, N = 2. (E) The quantification of deformation under different barrier modulation conditions. n (EGTA) = 22, N = 2; n (ZO1/2 dKD) = 10, N = 1. (F) Quantification of deformation under different ion channel inhibition conditions, all the inhibitors were administered before MHS deformations except for ouabain. ouabain n = 11, N = 1; Amiloride n = 21, N = 2; CFTR-172 n = 19, N = 2; Forskolin n = 15, N = 2; Ani9 n = 15, N = 2; Gd³⁺ n = 17, N = 2; Bumetanide n = 22, N = 2; EIPA n = 20, N = 1; CuSO₄ n = 9, N = 2.

the establishment of such gradients, the epithelial monolayer needs to establish proper barrier function associated with the establishment of an uninterrupted tight junction belt (28, 30). Immunostaining of ZO1 indeed revealed the formation of apical tight junctions in the epithelial cell monolayer (*SI Appendix*, Fig. S4). Furthermore, the perturbation of the barrier function by EGTA (3 mM), which destabilizes adherens and tight junctions (50), induced a complete relaxation of MHSs to their initial sizes (Fig. 3 C and E and *SI Appendix*, Fig. S5A). In line with this observation, we conducted experiments using MDCK ZO-1/2 double knockout (dKD) cells (51), which lack functional tight junctions. These cells showed no MHS compressing ability, demonstrating the necessity of an intact epithelial barrier for MHS compression to occur (Fig. 3 D and E and *SI Appendix*, Fig. S5B). Overall, our findings reveal that MHS compression is driven by an osmotic gradient and active water outflow generated by a polarized epithelial monolayer, functioning as a semipermeable membrane.

Active Transepithelial Transport Drives MHS Compression.

To better understand the active and passive polarized transport across the epithelial monolayer, we performed immunostaining on compressed MHS (*SI Appendix*, Fig. S6). The sodium–potassium pump Na⁺/K⁺-ATPase (NKA), which establishes essential electrochemical gradients for other ion channels (52), displayed

a distinct basolateral distribution. In contrast, the sodium–potassium–chloride cotransporter 1 (NKCC1), a key regulator of ion homeostasis in mammalian tissues (53), and the sodium–hydrogen exchanger 1 (NHE1), an important cell volume and pH regulator (54), were predominantly localized on the apical side.

To confirm that active transport across the epithelial monolayer drives MHS compression, we pharmacologically inhibited various ionic pumps and channels. Treatment with ouabain, a specific inhibitor of NKA, administered after MHS compression, resulted in significant MHS relaxation (Fig. 3F and *SI Appendix*, Fig. S7A). Conversely, amiloride, an inhibitor of the epithelial sodium channel, primarily involved in sodium reabsorption in kidney and lung epithelia, had no significant effect on MHS compression (Fig. 3F). Similarly, neither inhibition by cystic fibrosis transmembrane conductance regulator (CFTR)-172 nor activation by forskolin of the chloride channel CFTR, nor inhibition of another chloride channel, TMEM16A (55), by Ani9, nor inhibition of mechanosensitive ion channels by Gd³⁺ (38), affected MHS compression (Fig. 3F).

In contrast, inhibition of the sodium–potassium–chloride cotransporter NKCC1 with bumetanide significantly reduced MHS compression to 16.0 ± 3.1% compared to 18.7 ± 4.0% for controls, highlighting its critical role in the deformation process (Fig. 3F and *SI Appendix*, Fig. S7B). Similarly, inhibiting the NHE1 with EIPA led to a pronounced reduction in MHS

compression ($11.5 \pm 5.3\%$ compared to $18.7 \pm 4.0\%$ for controls) (Fig. 3F and *SI Appendix*, Fig. S7B). According to our hypothesis, transepithelial ion transport should drive passive water outflow facilitated by water channels such as aquaporins. Consistent with this, immunostaining showed aquaporin 3 (AQP3) localized in both basolateral and apical domains (*SI Appendix*, Fig. S6). Inhibition of AQP3 using CuSO₄ (56) caused a mild but significant reduction in MHS compression ($15.9 \pm 3.2\%$ compared to control conditions $18.7 \pm 4.0\%$) (Fig. 3F and *SI Appendix*, Fig. S7B). Altogether, these findings identify key ionic transporters and pumps involved in MHS compression. They provide compelling evidence that MHS compression results from active transepithelial ion transport, which generates osmotic and mechanical pressures essential for this process.

Tissue Maintains Long-Term Homeostasis after Reaching Mechanical Steady State. The decrease in MHS size resulted in a reduction in the epithelial monolayer surface area, averaging 37%. To investigate how this self-generated compression affects the epithelium organization and dynamics, we analyzed changes in cellular morphology before and after compression. Following MHS compression, we observed a major reduction in apical cell area ($214.0 \pm 105.1 \mu\text{m}^2$ at compressed state vs. $345.0 \pm 215.5 \mu\text{m}^2$ at the onset of compression), accompanied by an increase in cell height ($10.8 \pm 3.4 \mu\text{m}$ at compressed state vs. $6.8 \pm 2.9 \mu\text{m}$ at the onset of compression), indicative of a transition to a more columnar morphology (57, 58) (Fig. 4 A–C). Moreover, cell volume estimation computed from cell surface area and height revealed no statistically significant changes upon MHS deformation. Live imaging further revealed that cell height started

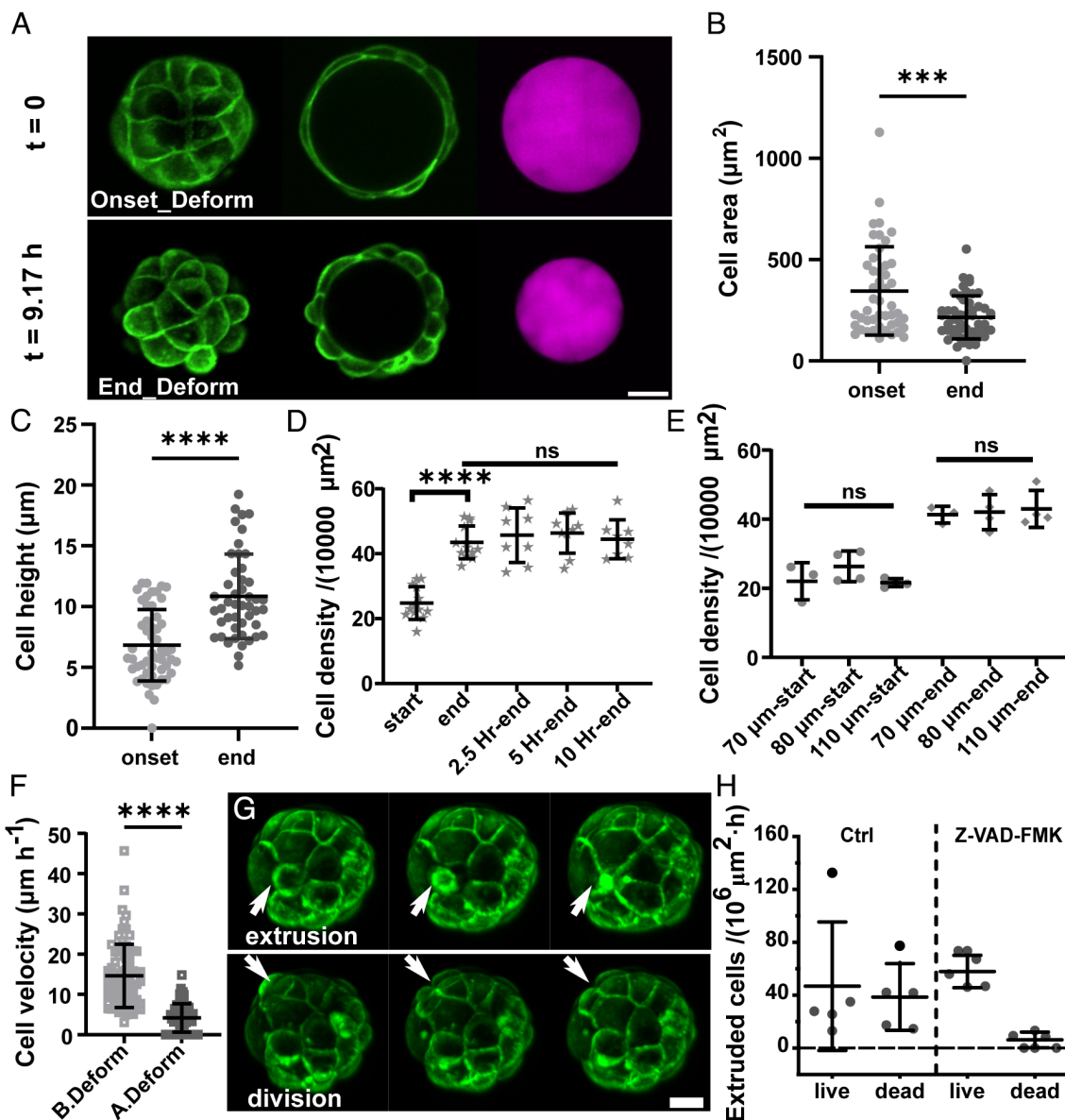


Fig. 4. Tissue homeostasis on the MHSs. (A) Representative evolution of MDCK CAAX-GFP cell morphology changes on MHS at the onset ($t = 0$ min) and the end ($t = 550$ min) of deformation, from left to right it shows the hemi-MHS z projection of cells, cells on the equatorial plane of the MHS, and corresponding MHS channel, respectively. (B) Cell area quantification at the onset and end of deformation. $n(\text{onset}) = 52$, $N = 4$; $n(\text{end}) = 47$, $N = 4$. (C) Cell height quantification at the onset and end of deformation. $n(\text{onset}) = 52$, $N = 4$; $n(\text{end}) = 47$, $N = 4$. (D) Cell density at the onset of deformation, the end of deformation and 2.5, 5, 10 h postdeformation, $n(\text{onset}) = 13$, $N = 2$; $n(\text{end}) = 13$, $N = 2$; $n(2.5 \text{ h-end}) = 8$, $N = 2$; $n(5 \text{ h-end}) = 9$, $N = 2$; $n(10 \text{ h-end}) = 8$, $N = 2$. (E) Cell density on MHS with varied initial sizes at the onset of deformation and the end of deformation. (F) Cell velocity quantification before and after deformation. $n(\text{B.Deform}) = 78$, $N = 2$; $n(\text{A.Deform}) = 61$, $N = 2$. (G) Representative cell extrusion and division events after MHS deformation. (H) Quantification of extruded cell fate expressed as frequency per unit area under control conditions and in Z-VAD-FMK treated conditions, $n(\text{ctrl}) = 5$, $N = 1$; $n(\text{Z-VAD-FMK}) = 5$, $N = 1$. (Scale bars, $20 \mu\text{m}$.)

to increase before confluence (*SI Appendix*, Fig. S8), indicative of a progressive maturation of the epithelium. During compression, cell morphological changes were purely geometrical since they occurred at constant cell volume. To further investigate the impacts of MHS compression on the epithelium, we measured cell densities at various time points: the onset of compression, the end of compression, and 2.5, 5-, and 10-h postcompression (Fig. 4D). Consistent with the reduction in apical cell area, cell density nearly doubled immediately after compression ($43.5 \pm 4.8 \text{ cell}/10^4 \mu\text{m}^2$) compared to the onset ($24.8 \pm 4.8 \text{ cell}/10^4 \mu\text{m}^2$). The density then remained stable for at least 3 d (Fig. 4D and *SI Appendix*, Fig. S9A), similar to that observed on 2D Polyacrylamide (PAAm) surfaces (*SI Appendix*, Fig. S9B). Interestingly, cell densities at both the onset and end of compression were independent of the initial MHS sizes, indicative of an intrinsic tissue property (Fig. 4E). Comparable density evolutions of Caco-2 epithelia on MHSs and on 2D substrates were also observed (*SI Appendix*, Fig. S9C and D). Additionally, live observations revealed a remarkable decrease in cell motility, from an average cell velocity of $14.6 \pm 7.8 \mu\text{m}/\text{h}$ before compression to $4.2 \pm 3.5 \mu\text{m}/\text{h}$ afterward (Fig. 4F). The concomitant decrease in cell motility and increase in cell density suggest that the 3D monolayers on MHSs transitioned to a homeostatic state.

Tissue crowding has been reported to induce cell extrusion (38, 59, 60). Performing live imaging, we observed a surge of cell extrusion events following MHS compression (Fig. 4G, *SI Appendix*, Fig. S10, and Movie S3). To investigate the fate of extruded cells, we labeled them with annexin V antibodies (60). Both live and dead cell extrusions were observed (Fig. 4H). Tissue homeostasis, as revealed by cell density maintenance over 3 d post-MHS compression (Fig. 4D and *SI Appendix*, Fig. S9), implies a balance between cell extrusion and division. Counting these events revealed indeed a balance between cell extrusion rates [$41 \pm 16 \text{ cells}/(10^6 \mu\text{m}^2 \cdot \text{h})$] and cell division rates [$41 \pm 18 \text{ cells}/(10^6 \mu\text{m}^2 \cdot \text{h})$] on compressed MHSs (*SI Appendix*, Fig. S11 and Movie S4). Interestingly, fluctuations in bead compression correlated with cell extrusion and division events (*SI Appendix*, Figs. S10 and S11), highlighting the dynamic nature of this self-regulated homeostatic state. To explore how the tissue adapts to perturbations, we inhibited apoptosis using Z-VAD-FMK (61). Apoptotic blockade induced a predominance of live-cell extrusions vs. dead cell extrusions, with however no significant effect on maximum MHS compression (Fig. 4H and *SI Appendix*, Fig. S12). These results suggest that the homeostatic control of the closed epithelial monolayer is a robust and adaptable process.

Our findings demonstrate that confluent epithelial tissue actively generates transepithelial fluid outflow, leading to the compression of the MHS it resides upon. This compression process is accompanied by tissue maintenance of close to *in vivo* homeostatic state, where cell division and extrusion are actively balanced.

A Spherically Symmetric Model for Tissue Mechanics and Hydraulic Properties Recapitulates the Experimental Data. To further determine the mechanisms at play, we developed a theoretical model that incorporates both tissue contractility and fluid transport. In this description, the cell height is neglected, and the epithelial cell monolayer is considered as a spherical semipermeable membrane of radius $R(t)$ enclosing a soft gel (MHS) (Fig. 5A).

We first discuss the mechanical properties of the system. The isotropic compression of the MHS results in an elastic stress proportional to the relative deformation that reads $3B(R_0 - R(t))/R_0$ where B is the gel bulk modulus and $R_0 = R(t=0)$ is the radius of the MHS prior to compression. This isotropic stress must be balanced by the Laplace pressure contribution $2\Gamma/R(t)$ where Γ

is the tissue surface tension stemming mainly from the acto-myosin cortex contractility, and by the mechanical pressure difference $P^{in} - P^{out}$ between the inside and the outside of the tissue layer. Force balance thus reads:

$$P^{in} - P^{out} + 3B \frac{R_0 - R(t)}{R_0} = \frac{2\Gamma}{R(t)}. \quad [1]$$

To account for active tissue pumping, an irreversible thermodynamics framework (62, 63) is used. Cells actively pump ions, which in turns creates an osmotic pressure difference leading to (passive) water flux. Water flux is thus driven by two thermodynamic forces: mechanical and osmotic pressure differences, such that the sphere volume $V(t) = 4\pi R(t)^3/3$ dynamics obeys:

$$\frac{dV}{dt} = A\lambda[(P^{out} - P^{in}) - \sigma(\Pi^{out} - \Pi^{in})], \quad [2]$$

where $A = 4\pi R(t)^2$ denotes the sphere surface area, λ is the tissue permeability to water flows, and $\Pi^{out} - \Pi^{in} = -k_B T \Delta C$ with $\Delta C = C^{in} - C^{out}$ denotes the osmotic pressure difference across the epithelium. Particularly, we have included a reflection/selectivity coefficient σ (63, 64). A fully semipermeable membrane that allows only water to pass corresponds to $\sigma = 1$, while a fully permeable membrane that is permeable to both water and osmolytes has $\sigma = 0$. When accounting for ion diffusion, which may influence the generated osmotic pressure, we determined that ion concentrations within the MHS reach homogeneity on a timescale of approximately 1 s. By contrast, equilibration in the outer medium requires up to 40 h. Incorporating diffusion into the model results in a slightly accelerated compression but does not substantially affect the overall conclusions (*SI Appendix*, *Theoretical Model and Supporting Calculations*). Accordingly, in the subsequent analysis, we assume that the concentrations C^{in} and C^{out} are homogeneous within the MHS and the outer medium, respectively.

Finally, an osmotic pressure difference builds up due to cell active pumping. For simplicity, we consider here the transport of a single ionic species. The number N^{in} of ions in the sphere evolves according to

$$\frac{dN^{in}}{dt} = A \left[\Lambda_i (\mu^{out} - \mu^{in}) + (1 - \sigma) C^{out} \frac{dV}{dt} - J^p \right], \quad [3]$$

where Λ_i is the Onsager coefficient for ion transport through the membrane, $\mu^{out} - \mu^{in} \approx -k_B T \Delta C / C^{out}$ denotes the chemical potential difference between the outside and inside and J^p is the flux due to active transport (positive when directed outward).

This system of equations captures sphere compression with a stable steady-state radius $R^* < R_0$ when the active ion flux is directed outward ($J^p > 0$), or sphere expansion when the active ion flux is directed inward ($J^p < 0$) and surface tension is sufficiently low. Fig. 5B displays a state diagram of our model for different values of the parameters. In our experimental system, robust MHS compressions are observed, corresponding to the epithelial active transport being directed outward ($J^p > 0$), increasing the concentration outside and therefore creating a non-vanishing osmotic pressure difference which leads to water efflux from the MHS. The normalized steady-state diameter can be obtained from our model and reads:

$$D^*/D_0 = \left[1 - C^{out} J + \sqrt{(1 - C^{out} J)^2 - 8\gamma} \right] / 2, \quad [4]$$

where $J = \sigma J^p / 3B\Lambda_i$ and $\gamma = \Gamma / 3BR_0$. We then fitted Eq. 4 using experimental data for different osmotic conditions (Fig. 5C),

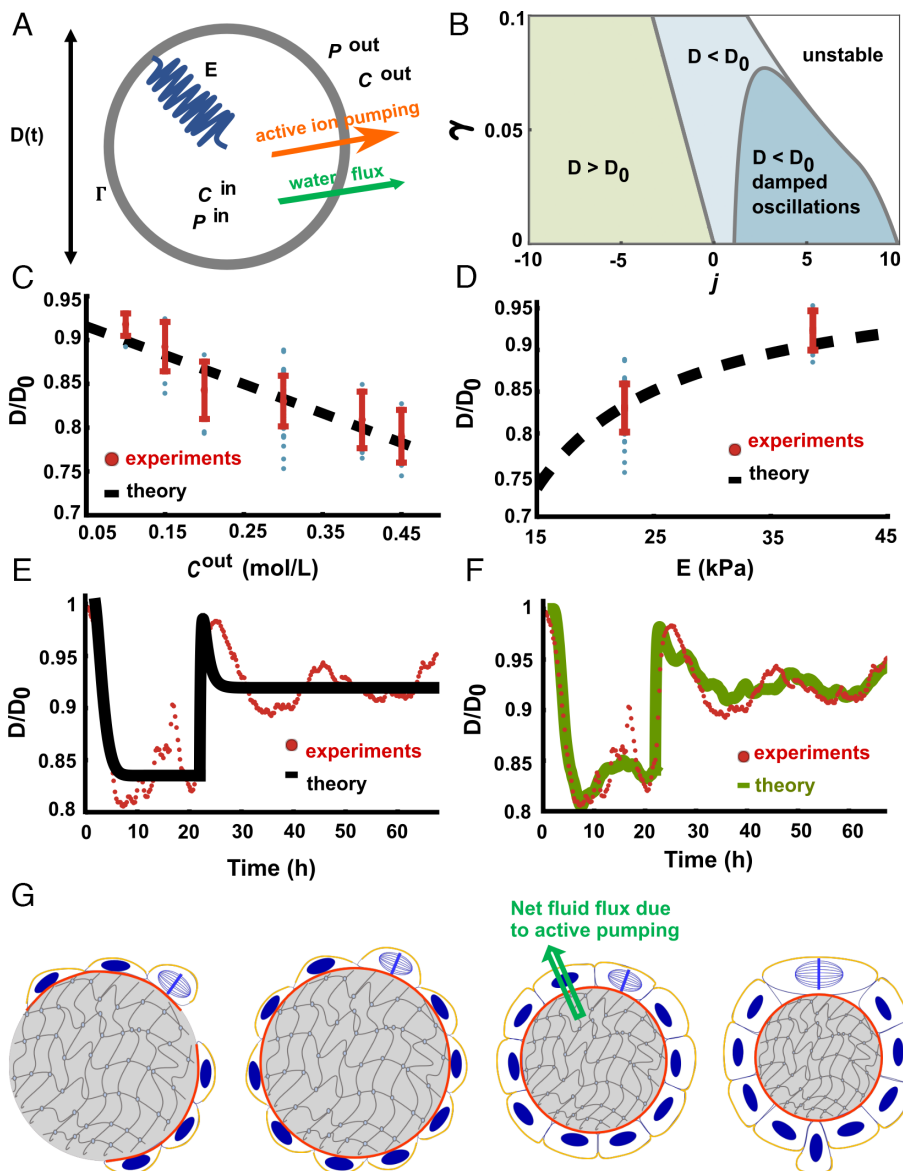


Fig. 5. Mechanohydraulic model of a tissue monolayer. (A) Schematics of the theoretical model. Cells actively pump ions from the basal to apical side (orange-color arrow), which leads to a water efflux (green arrow) following osmotic pressure difference. This water efflux results in gel compression thus generating a compressive stress, which is symbolized by a spring. (B) State diagram of the model for different values of the dimensionless pumping $j = \sigma^0 C^{out}/3B\Lambda_i$ and surface tension $\gamma = \Gamma/3BR_0$. (C) Normalized steady-state diameter D/D_0 as function of the medium concentration C^{out} (in mol/L). The black dashed line is a fit of Eq. 4 to the experimental data (dots). Fitted values: $j = \sigma^0 C^{out}/3B\Lambda_i = 3.310^{-1}$ L/mol and $\gamma = \Gamma/3BR_0 = 3.810^{-2}$ (dimensionless). (D) Normalized steady-state diameter D/D_0 as function of the gel Young's modulus E (in kPa). The black dashed line is a prediction from equation using the values fitted in (C). (E) Normalized diameter $D(t)/D_0$ as function of time during an osmotic shock experiment (red dots). The black line shows the corresponding dynamics obtained from fitting the theoretical model. (F) Normalized diameter $D(t)/D_0$ as function of time during an osmotic shock experiment (red dots, same data as in E). The green solid line shows a realization of the stochastic model (picked among 1,000 realizations) that resembles the experimental data. (G) Schematics representing the whole self-regulated homeostasis process due to active fluid transport in epithelial tissue. See *SI Appendix* for details.

thus obtaining $J = 3.3 \cdot 10^{-1}$ L/mol and $\gamma = 3.8 \cdot 10^{-2}$ (dimensionless) which are in agreement with literature values (62, 63). Note that we have considered a constant Onsager coefficient Λ_i rather than a constant membrane permeability to ion flows $\Lambda = k_B T \Lambda_i / C^{out}$. This choice yields the correct concentration dependence of the steady-state diameter.

Without further fitting, Eq. 4 was then used to predict the steady-state radius for different MHS stiffnesses, and a remarkable agreement was shown with the experimental results (Fig. 5D). The fitted parameters from osmotic shock experiments (Fig. 5C) accurately capture the dependence of the steady-state radius on gel stiffness, especially for stiffer gels. However, additional experiments revealed a deviation at low stiffness (5.2 kPa), where tissues

compressed less than expected (*SI Appendix*, Fig. S13E), suggesting that epithelial hydraulic properties themselves depend on the substrate stiffness, likely through reduced pumping or increased leakage.

We then compared the dynamics predicted by our model to the experimental ones. An example of this comparison is displayed in Fig. 5E for the case of an osmotic shock where the outer medium is diluted from $C^{out} = 0.3$ mol/L to $C^{out} = 0.1$ mol/L during the experiment. The fitting shows a good agreement with the first compression stage. Similarly, good fits are obtained for other osmotic shock experiments. Note however that the model accounts neither for the slower relaxation to the steady state that follows the osmotic shock, nor for the overall large fluctuations around the steady-state radius.

As shown in the experiments, the compression of MHS is coupled with cell density changes, and we thus further extended our model by including cell density fluctuations. The compression leads to an increase in cell density and enables a homeostatic state to be achieved rapidly. Therefore, close to the homeostatic state, we write the dynamics for the cell density $\varrho(t)$ as a Langevin equation (see *SI Appendix* for details):

$$\frac{1}{\varrho_h} \frac{d\varrho}{dt} = -\frac{\varrho}{\varrho_h} \frac{dA/dt}{A} + \frac{1}{\tau} \left(1 - \frac{\varrho}{\varrho_h}\right) + \xi(t), \quad [5]$$

where ϱ_h is the homeostatic cell density. In Eq. 5, the first term on the right-hand side accounts for density variations due to MHS surface area changes, the second one for the relaxation to the homeostatic state with characteristic time τ , and the last term $\xi(t)$ is a stochastic Gaussian white noise with vanishing mean and variance $\langle \xi(t)\xi(t') \rangle = 2W \delta(t-t')$, where the noise amplitude W is expected to scale as $1/N$ where N is the number of cells. The feedback of cell density fluctuations to the mechanohydraulic model then takes the form of a density-dependent surface tension:

$$\Gamma(\varrho) = \Gamma_0 \left[1 - \alpha \left(1 - \frac{\varrho}{\varrho_h} \right) \right], \quad [6]$$

where α is a dimensionless parameter and Γ_0 is the surface tension at the homeostatic density. For $\alpha > 0$, which we consider in the following, the tissue surface tension is lowered ($\Gamma(\varrho) < \Gamma_0$) whenever the tissue density is smaller than its homeostatic density ($\varrho < \varrho_h$).

An example of realization of the stochastic mechanohydraulic model given by Eqs. 1–3, 5, and 6 is provided in the *SI Appendix* (Fig. S17). Large fluctuations around the mean steady-state radius, similar to those in the experiments, are observed. Those large fluctuations can be understood as a consequence of the positive feedback between density changes and surface tension: If a cell density fluctuation lower ϱ , it causes a lowering of the surface tension, which itself favors an increase of the radius and thus a further decrease of the cell density.

Finally, we return to the experimental data and compare our stochastic model to osmotic shock experiments. Notably, adding stochastic cell division/extrusion and their mechanical feedback leads to radius fluctuations that are similar to those observed experimentally (Fig. 5F). In addition, the stochastic model also accounts for the slower relaxation to the steady state that follows the osmotic shock. As an alternative to the density dependence of the surface tension in Eq. 6, we have considered other mechanisms by which density fluctuations could feedback on the hydraulic model. Since cell divisions or extrusions could trigger leakage (26, 27), we have also considered a density dependence of the Onsager coefficient Λ_i or of the permeability to water λ . In the *SI Appendix*, we show that a density-dependent Onsager coefficient Λ_i leads to similar results as a density-dependent surface tension. On the other hand, a density-dependent permeability to water flow only plays a role while the sphere volume is changing and thus does not generate radius fluctuations as observed in the experiments.

In summary, utilizing a simplified stochastic mechanical-hydraulic theoretical model, we managed to recapitulate the experimental observations, which validates our experimental conclusions. In particular, we note that the fitted dimensionless surface tension γ is indeed small and its contribution to the MHS compression is negligible compared to the role of ion pumping that leads to an osmotic pressure difference. This is also in agreement with the experimental observation that the Na⁺/K⁺-ATPase inhibition by ouabain leads to the most drastic reduction of the MHS compression: From the model perspective, inhibiting this pump means a

smaller value of the parameter J^0 in Eq. 3, which results in smaller steady-state diameter according to Eq. 4. In addition, the theoretical model provided an interesting perspective on the relationship between tissue surface tension and corresponding cell density, which can be useful in future studies.

Discussion

Our study uncovers a hydraulic origin of stress generation in epithelial tissues. Using MHSs as a boundary-free model, we show that epithelia are capable of generating large isotropic compressive stresses, on the order of several kilo-Pascals, through active ion transport and subsequent water efflux. This finding challenges the long-standing view that acto-myosin contractility is the dominant driver of epithelial mechanics and suggests that hydraulic processes play a much larger role in tissue homeostasis than previously recognized.

Compared to prior reports on stresses generated by tissue hydraulics (26, 33, 48, 65), the stresses we measured here exceed them by more than an order of magnitude. In our system, the measured pressure reflects gel compression rather than hydrostatic pressure. Active basal-to-apical ion pumping generates an osmotic gradient that drives water efflux from the MHS, compressing the gel until osmotic and gel compression generated mechanical stresses equilibrate at ~7 kPa. This compression also affects the MDCK monolayer, reinforcing columnar cell packing, tight junctions and barrier integrity, which explains the quasi-stable MHS size observed postdeformation. By contrast, in other systems such as domes and cysts, the accumulation of fluid stretches the cell monolayer, thus resulting in weakened cell–cell junctions that lead to junctional fracture which prevent higher pressure build-up, which could explain the observed cycle of inflation/deflation. In 2D systems, the previously reported lower pressures may result from fluid leaks that prevent osmotic gradients from building up. In addition, in cysts, underestimation could also be methodological: Pipette aspiration measures local cortical tension rather than osmotic pressure, while efflux-based assays after puncture can underestimate pressure if the surrounding medium is porous and dissipates flow.

Our results also highlight a striking functional outcome: Self-generated compression drives epithelia to a defined homeostatic state. The active ion transport and water efflux led to a self-compression of the monolayer by ~37%, resulting in a homeostatic cell density that remained stable for at least 3 d, indicating that tissue self-compression achieved a transition to a preferred homeostatic density. Caco-2 epithelia behaving similarly in maintaining cell density post-MHS compression, suggests that active fluid transport may serve as a general regulator of epithelial homeostasis across tissues. Notably, this cell density was independent of MHS size, indicating that it was an intrinsic tissue property. Unlike externally applied compression, which induces transient density changes and often destabilizes tissues (38), transport-mediated self-compression produced a stable balance of proliferation and extrusion. Both live and dead cell extrusion were observed at higher rates than in 2D cultures (59), with a greater proportion of live cell extrusions (60). The observed increase in live-cell extrusion when apoptotic extrusion was inhibited without effect on self-compression further indicates that homeostasis is regulated independently of specific extrusion mechanisms.

This rapid establishment of homeostasis could not be achieved by proliferation alone, but was facilitated by active basal-to-apical fluid transport (Fig. 5G). Indeed, during self-compression, the epithelium reached a twofold increase in cell density in 6 h on average which is at least three times faster than would be possible

through proliferation alone, which typically requires 18 to 24 h (47). A particularly interesting aspect of this process is the directionality of fluid transport. MDCK epithelial tissues are known to transport fluid in both directions: basal to apical and apical to basal, depending on culture conditions. In conventional 2D cultures, whether on impermeable substrates (such as plastic, glass, and PDMS) (65) or permeable supports (such as Transwell) (48), MDCK monolayers typically show net apical to basal transport. In contrast, 3D culture systems often display bidirectional transport. For example, MDCK cysts in suspension cultures generally transport from apical to basal, resulting apical-out cysts, whereas ECM-embedded cysts exhibit basal to apical transport, forming basal-out cysts (32). The factors that determine transport direction in these systems remain unclear, and further studies are needed to elucidate the underlying mechanisms.

To address the question of how fluid transport couples to mechanics at the tissue level, our modeling shows that even a small total transepithelial ion concentration difference ($C^{in} - C^{out} \approx -3$ mM) is sufficient to drive water efflux and counter balance the compressive mechanical stress generated by MHS. Importantly, the model reveals that epithelia cannot be treated as ideal semipermeable membranes. Instead, cross-coupling between ion and water fluxes that arise from paracellular pathways (66) and cotransport (67) processes must be considered. While a cell-level description of hydraulic processes is needed to capture cell shape changes during MHSs compression, the present framework already establishes a quantitative basis for connecting cell-level transport activity to emergent tissue-scale mechanics and offers a platform for predicting how epithelial geometry and density influence mechanical stress generation.

In vivo, epithelia in organs such as the kidney and intestine routinely handle large transepithelial fluxes (68, 69). Our findings imply that these transport processes may also contribute to the mechanical regulation of tissue homeostasis, complementing or even surpassing the role of contractility in certain contexts. We thus identify active ion transport as a powerful source of epithelial mechanical stress that enables tissues to achieve and maintain density homeostasis. By shifting the focus from contractility to hydraulics, our work expands the conceptual framework of epithelial mechanics and points toward fluid transport as a key regulator of tissue behavior.

Materials and Methods

Cell Line Origin and Maintenance. The MDCK cell lines MDCK Histone H1 GFP (70), MDCK LifeAct GFP (60), MDCK NMMIIA KD (44), and MDCK ZO-1/2 dKD (51) were used. To obtain MDCK CAAX-GFP cells, MDCK cells were transfected by electroporation using NeonTM Transfection System (Thermo Fisher, 100 μ L reaction kit, Ref MPK10096, 1,650 V, 20 ms, 1 pulse). The stable MDCK CAAX-GFP clone was selected after two rounds of fluorescence-activated cell sorting. All MDCK cell lines were cultured in Dulbecco's modified eagle medium with 4.5 g/L glucose and L-glutamine (DMEM, Gibco, 31966-021) and 1% penicillin-streptomycin (Gibco, 14140-112), containing 10% fetal bovine serum (BioWest, Cat# S1810-500), (denoted as DMEM-FBS) media at 37 °C incubators supplemented with 5% CO₂. Caco-2 cells (from ATCC) were cultured at 37 °C incubators supplemented with 5% CO₂ in the same DMEM but containing 20% FBS.

Fabrication of MHSs. The MHSs were fabricated using a water-in-oil emulsion protocol as summarized in *SI Appendix, Fig. S1A*; 20 μ L aqueous PEGDA (mw. 700 Da, Sigma, Cat.455008) solution containing 10% PEGDA (MHS), 7% (for MHS_soft), or 15% (for MHS_stiff), 0.3 mg/mL photoinitiator Irgacure® 2959 (BASF, Cat.55047962), 0.2% surfactant sodium dodecyl sulfate (Euromedex, EU0660), 0.05 mg/mL fibronectin (Merck Millipore, FC010), and 0.2 mM acryloyloxyethyl thiocarbamoyl rhodamine B (Acryl-RhoB, Polysciences, Cat.25404) was added to 1 mL mineral oil (Sigma, Cat.M8410), followed by 1 min of vortex

and 30 s of UV illumination. Then, 2 mL DMEM-FBS medium was added to the emulsion with subsequent centrifugation at 1,000 rpm for 3 min to precipitate the formed MHSs. Several DMEM wash and centrifugation processes were conducted to completely remove the mineral oil, then the MHSs were kept in DMEM and incubated at 37 °C until being used.

Cell Seeding on MHSs. After trypsin (Gibco, 25300-054) treatment, cells are centrifuged and resuspended in DMEM-FBS, then the cells are mixed with prepared MHSs at a desired cell density in a low adhesion plate. After 1 to 2 h of incubation, the MHSs are washed with fresh DMEM_C medium to remove the nonadhered cells.

PAA Gel Fabrication. 21 kPa PAAm gels were prepared as described previously (73). The PAAm gels were washed with 10 mM 4-(2-Hydroxyethyl)-1-piperazin eethanesulfonic acid and coated with a 50 μ g/mL fibronectin solution prior to cell seeding.

Drug Treatments. During time-lapse imaging process, warm DMEM-FBS containing certain drug (first dissolved in Dimethyl Sulfoxide at high concentration and then diluted 1,000 times with culture medium to the final concentrations as indicated in *SI Appendix, Table S1*) was added into the live imaging sample after removing the pure DMEM-FBS at certain time point. All those manipulations were conducted in between the acquisition intervals, therefore imposed no change to the registered data points and acquisition settings. The details of used drugs can be found in *SI Appendix, Table S1*.

Live Imaging. Cell-laden MHSs are resuspended in DMEM-FBS, then mixed with 1% liquefied agarose gel at a temperature around 37 °C quickly and gently with a volume ratio of 1:1, then poured to a glass-bottom petri dish and allowed the gelling of agarose gel at room temperature (RT) for 3-5 min before adding DMEM-FBS. The prepared samples are incubated at 37 °C for at least 2 h before live microscopic observations. Time-lapse live images were performed either on a multichannel inverted microscope (Olympus, IX83) equipped with temperature and CO₂ control box or on a high-resolution spinning disk microscope (Nikon, Ti2 Eclipse) equipped with temperature and CO₂ control box. Multiple (x, y) positions, z stacks (1 to 3 μ m per step, 12 to 120 steps in total) and multichannels were utilized to obtain the precise MHS sizes and/or cellular activities.

MHSs Deswelling Experiments. Fabricated MHSs were first encapsulated in 0.5% agarose gel and incubated in DMEM-FBS at 37 °C for more than 24 h to reach an equilibrium swelling state. Then, the MHSs were imaged with a high-resolution spinning disk microscope (Nikon, Ti2 Eclipse) under the condition of live cell imaging to reveal the original MHS sizes. Then, the sample is rinsed more than three times using DMEM-FBS containing extra NaCl of various concentrations, followed by a more than 24 h incubation to ensure equilibrium swelling of the MHS at 37 °C before spinning disk imaging. The incubation of MSHs in different media followed a fashion where NaCl concentration changed from low to high (1 to 5+ M), and the obtained sizes were normalized by the original MHS size.

Osmotic Shock Experiments. MDCK cells were seeded on MHSs then under live-imaging in normal osmolarity conditions. After the MHSs were deformed, pre-warmed new medium with varied osmolarities was added into the samples after carefully removing the old medium. The shocks were applied in between acquisition intervals therefore no other experimental parameters were modified except for medium osmolarity. To prepare osmotic shock media, 100 mM sucrose and 150 mM NaCl were added to physiological culture medium (300 mM) to obtain hypertonic shock media of 400 mM and 450 mM, respectively; 1 mL, 1.5 mL, and 2 mL Milli Q water were added to 2 mL, 1.5 mL, and 1 mL physiological culture medium to obtain 200 mM, 150 mM, and 100 mM hypotonic shock media, respectively.

Indentation Experiments. 2D PEGDA gels with the same formulation as PEGDA MHSs were equilibrated in DMEM_C media before indentation were performed with a nanoindenter (Chiao, Optics11 Life) mounted on an inverted multichannel microscope (Olympus, IX83) at room temperature, with a spherical tip of 9 μ m and a cantilever stiffness of 0.53 N/m. The indentation depth was set at 1.5 μ m and acquired data were fitted with Hertz model to obtain the Young's modulus E. At least three parallel samples were measured for each rigidity. At least 10 static measurements on different regions of the sample were performed for each sample.

Compressive Stress Evaluation. The compressive stress (ΔP) required to deform isotropically a homogenous material can be evaluated from the bulk modulus (B) of the material using the following relation (71):

$$B = \left| \frac{\Delta P}{\Delta V/V} \right|,$$

where V is the initial volume of the material and ΔV is the volume change of the material. In our experiments, the bulk moduli B of the MHS exhibiting two different rigidities are calculated according to the following relation:

$$B = \frac{E}{3(1-2\nu)},$$

where E is the Young's modulus (obtained from indentation experiments), and ν is the Poisson ratio. According to the study by J. Cappello et al. (72), the MHSs for both rigidities have an estimated Poisson's ratio of $\nu \approx 0.25$.

Volumetric Flux Calculation. The average volumetric flux or water flux rate per unit area q was estimated from the MHS compression as follows:

$$q = \frac{1}{A_{\text{average}}} \frac{\Delta V}{\Delta T},$$

where ΔV is the volume loss of the MHS during the duration ΔT of the deformation, and A_{average} is the averaged compression-onset and compression-end surface area of MHS.

Immunostaining and Confocal Imaging. Cell adhered MHSs at different time points/tissue growing stages are fixed and stained by immuno-fluorescence with a modified paraformaldehyde (PFA) protocol, details of used agents and antibodies can be found in [SI Appendix, Table S1](#).

Briefly, samples embedded in agarose gels were fixed with 4% PFA in Phosphate-Buffered Saline (PBS) (30 min, room temperature), washed three times for 3 to 5 min with PBS then stored in PBS at 4 °C overnight. Next day, the samples were taken out and let to warm up to room temperature. Then, the samples were permeabilized with 0.5% Triton in PBS (30 min, room temperature) and blocked (1% BSA in PBS) for 2 h followed by 15 min wash in PBS. Samples were subsequently incubated overnight at 4 °C with primary antibodies in blocking buffer under agitation. The next day, they were washed with PBS for three times, 10 min each. Samples were then incubated with secondary antibody at room temperature for 3 h under agitation, followed by extensive washing in PBS. Then, the samples were mounted with Vectashield mounting media on cover slides and sealed with dental glue for imaging, using either a Zeiss LSM 980 Airyscan confocal microscope with glycerin immersion objectives (25× or 40×) at 0.5 to

1 μm per stack, or a Nikon Ti2 Eclipse spinning disk confocal microscope with 20× air objective at 0.3 to 1 μm per stack.

Data Analysis. All the images (including time-lapse live image) obtained were either analyzed by Fiji, Imaris (10.1.1) or CellPose2. The statistics obtained from image analysis and other measurements were processed either by Origin (2017) or GraphPad (Prism 9 or 10). Sigmoid fitting analysis was performed first using MATLAB and further processed by GraphPad (Prism 10). Unless otherwise indicated, all plots show the Mean ± SD. P -values were calculated by the t test, ns $P > 0.05$, * $P < 0.05$, ** $P < 0.01$, *** $P < 0.001$, and **** $P < 0.0001$.

Specifically, segmentation of confocal images showing cell apical membrane marker (either MDCK CAAx-GFP or E-cadherin GFP) were conducted using CellPose2, then cell areas were quantified according to the segmentation using Fiji. Note that the curvature of MHS was not taken into account. Cell heights were quantified manually using Fiji tools, the highest point of a cell was extracted over a whole z-stack image. Cell displacement on the MHSs was manually quantified over live cell imaging videos, note that the curvature of the MHS was not taken into account, thereby expressing underestimated cell velocities.

Data, Materials, and Software Availability. All study data are included in the article and/or [supporting information](#).

ACKNOWLEDGMENTS. We would like to thank Joseph d'Alessandro for some codes, as well as all the members of the "Cell adhesion and Mechanics" team for helpful discussions. This work was supported by the European Research Council (Grant No. Adv-101019835 to B.L.), LABEX Who Am I? (ANR-11-LABX-0071 to B.L. and R.-M.M.), the Ligue Contre le Cancer (Equipe labellisée 2019 to R.-M.M.), the Alexander von Humboldt Foundation (Alexander von Humboldt Professorship to B.L.), Institut National du Cancer (INCa_16712 and INCa_18429 to B.L. and R.-M.M.), and the Agence Nationale de la Recherche ("STRATEPI" DFG-ANR-22-CE92-0048 to R.-M.M.). We acknowledge the ImagoSeine core facility of the IJM, a member of IBISA and France-Biolimaging (ANR-10-INBS-04) infrastructures.

Author affiliations: ^aCNRS, Institut Jacques Monod, Université Paris Cité, Paris 75913, France; ^bLaboratoire Physique des Cellules et Cancer, CNRS UMR 168, Institut Curie, Université Paris Sciences et Lettres, Sorbonne Université, Paris 75005, France; ^cDepartment of Physics, Friedrich-Alexander Universität Erlangen-Nürnberg, Erlangen 91058, Germany; and ^dMax Planck Institute for the Science of Light and Max-Planck-Zentrum für Physik und Medizin, Erlangen 91054, Germany

Author contributions: C.D., B.L., and R.-M.M. designed research; H.W., G.A., R.C., and T.D. performed experimental research; C.D. and J.P. developed the theoretical model; H.W., C.D., G.A., R.C., T.D., J.P., B.L., and R.-M.M. analyzed data; and H.W., C.D., B.L., and R.-M.M. wrote the paper.

1. C. Guillot, T. Lecuit, Mechanics of epithelial tissue homeostasis and morphogenesis. *Science* **340**, 1185–1189 (2013).
2. N. Gorfinkel, G. B. Blanchard, Dynamics of actomyosin contractile activity during epithelial morphogenesis. *Curr. Opin. Cell Biol.* **23**, 531–539 (2011).
3. R. Sunyer *et al.*, Collective cell durotaxis emerges from long-range intercellular force transmission. *Science* **353**, 1157–1161 (2016).
4. M. J. Paszek *et al.*, Tensional homeostasis and the malignant phenotype. *Cancer Cell* **8**, 241–254 (2005).
5. A. Proag, B. Monier, M. Suzanne, Physical and functional cell-matrix uncoupling in a developing tissue under tension. *Development* **146**, dev172577 (2019).
6. A. Elosegui-Artola *et al.*, Matrix viscoelasticity controls spatiotemporal tissue organization. *Nat. Mater.* **22**, 117–127 (2023).
7. S. Sonam *et al.*, Mechanical stress driven by rigidity sensing governs epithelial stability. *Nat. Phys.* **19**, 132–141 (2023).
8. S. P. Pothapragada, P. Gupta, S. Mukherjee, T. Das, Matrix mechanics regulates epithelial defence against cancer by tuning dynamic localization of filamin. *Nat. Commun.* **13**, 218 (2022).
9. B. Ladoux, R.-M. Mège, Mechanoobiology of collective cell behaviours. *Nat. Rev. Mol. Cell Biol.* **18**, 743–757 (2017).
10. A. Shellard, R. Mayor, Supracellular migration—Beyond collective cell migration. *J. Cell Sci.* **132**, jcs226142 (2019).
11. P. Agarwal, R. Zaidel-Bar, Principles of actomyosin regulation in vivo. *Trends Cell Biol.* **29**, 150–163 (2019).
12. C. De Pascalis, S. Etienne-Manneville, Single and collective cell migration: The mechanics of adhesions. *Mol. Biol. Cell* **28**, 1833–1846 (2017).
13. G. Charras, A. S. Yap, Tensile forces and mechanotransduction at cell-cell junctions. *Curr. Biol.* **28**, R445–R457 (2018).
14. H. Wolfenson, B. Yang, M. P. Sheetz, Steps in mechanotransduction pathways that control cell morphology. *Annu. Rev. Physiol.* **81**, 585–605 (2019).
15. K. M. Stroka *et al.*, Water permeation drives tumor cell migration in confined microenvironments. *Cell* **157**, 611–623 (2014).
16. M. Guo *et al.*, Cell volume change through water efflux impacts cell stiffness and stem cell fate. *Proc. Natl. Acad. Sci. U.S.A.* **114**, E8618–E8627 (2017).
17. C. M. Nelson *et al.*, Microfluidic chest cavities reveal that transmural pressure controls the rate of lung development. *Development* **144**, 4328–4335 (2017).
18. J. Ferenc *et al.*, Mechanical oscillations orchestrate axial patterning through Wnt activation in Hydra. *Sci. Adv.* **7**, eabj6897 (2021).
19. J. G. Dumortier *et al.*, Hydraulic fracturing and active coarsening position the lumen of the mouse blastocyst. *Science* **365**, 465–468 (2019).
20. M. I. Choudhury, M. A. Benson, S. X. Sun, Trans-epithelial fluid flow and mechanics of epithelial morphogenesis. *Semin. Cell Dev. Biol.* **131**, 146–159 (2022).
21. M. Chugh, A. Munjal, S. G. Megason, Hydrostatic pressure as a driver of cell and tissue morphogenesis. *Semin. Cell Dev. Biol.* **131**, 134–145 (2022).
22. N. T. Chartier *et al.*, A hydraulic instability drives the cell death decision in the nematode germline. *Nat. Phys.* **17**, 920–925 (2021).
23. A. Stokkermans *et al.*, Muscular hydraulics drive larva-polyp morphogenesis. *Curr. Biol.* **32**, 4707–4718.e8 (2022).
24. A. Munjal, E. Hannezo, T. Y. C. Tsai, T. J. Mitchison, S. G. Megason, Extracellular hyaluronate pressure shaped by cellular tethers drives tissue morphogenesis. *Cell* **184**, 6313–6325.e18 (2021).
25. J. Firmin *et al.*, Mechanics of human embryo compaction. *Nature* **629**, 646–651 (2024).
26. C. J. Chan *et al.*, Hydraulic control of mammalian embryo size and cell fate. *Nature* **571**, 112–116 (2019).
27. T. Ruiz-Herrero, K. Alessandri, B. V. Gurchenkov, P. Nassoy, L. Mahadevan, Organ size control via hydraulically gated oscillations. *Development* **144**, 4422–4427 (2017).
28. N. L. Simmons, Ion transport in 'tight' epithelial monolayers of MDCK cells. *J. Membr. Biol.* **59**, 105–114 (1981).
29. W. Van Diessche, W. Zeiske, Ionic channels in epithelial cell membranes. *Physiol. Rev.* **65**, 833–903 (1985).
30. O. Kovbasnjuk, J. P. Leader, A. M. Weinstein, K. R. Spring, Water does not flow across the tight junctions of MDCK cell epithelium. *Proc. Natl. Acad. Sci. U.S.A.* **95**, 6526–6530 (1998).

31. T. Otani *et al.*, Claudins and JAM-A coordinately regulate tight junction formation and epithelial polarity. *J. Cell Biol.* **218**, 3372–3396 (2019).
32. A. Z. Wang, G. K. Ojakian, W. J. Nelson, Steps in the morphogenesis of a polarized epithelium: I. Uncoupling the roles of cell-cell and cell-substratum contact in establishing plasma membrane polarity in multicellular epithelial (MDCK) cysts. *J. Cell Sci.* **95**, 137–151 (1990).
33. M. Mukenhirn *et al.*, Tight junctions control lumen morphology via hydrostatic pressure and junctional tension. *Dev. Cell* **59**, 2866–2881.e8 (2024).
34. S. Dasgupta, K. Gupta, Y. Zhang, V. Viasnoff, J. Prost, Physics of lumen growth. *Proc. Natl. Acad. Sci. U.S.A.* **115**, E4751–E4757 (2018).
35. J. E. Tanner, Intracellular diffusion of water. *Arch. Biochem. Biophys.* **224**, 416–428 (1983).
36. S. Fernández-Castelo, J. J. Bolívar, R. López-Vancell, G. Beaty, M. Cereijido, "Ion transport in MDCK cells" in *Tissue Culture of Epithelial Cells*, M. Taub, Ed. (Springer, US, Boston, MA, 1985), pp. 37–50, 10.1007/978-1-4684-4814-6_3.
37. L. Casares *et al.*, Hydraulic fracture during epithelial stretching. *Nat. Mater.* **14**, 343–351 (2015).
38. G. T. Eisenhoffer *et al.*, Crowding induces live cell extrusion to maintain homeostatic cell numbers in epithelia. *Nature* **484**, 546–549 (2012).
39. E. Marinari *et al.*, Live-cell delamination counterbalances epithelial growth to limit tissue overcrowding. *Nature* **484**, 542–545 (2012).
40. L. Trichet *et al.*, Evidence of a large-scale mechanosensing mechanism for cellular adaptation to substrate stiffness. *Proc. Natl. Acad. Sci. U.S.A.* **109**, 6933–6938 (2012).
41. D. Mitrossilis *et al.*, Real-time single-cell response to stiffness. *Proc. Natl. Acad. Sci. U.S.A.* **107**, 16518–16523 (2010).
42. A. Elosegui-Artola *et al.*, Mechanical regulation of a molecular clutch defines force transmission and transduction in response to matrix rigidity. *Nat. Cell Biol.* **18**, 540–548 (2016).
43. A. Cavallo, M. Madaghieh, U. Masullo, M. G. Lionetto, A. Sannino, Photo-crosslinked poly(ethylene glycol) diacrylate (PEGDA) hydrogels from low molecular weight prepolymer: Swelling and permeation studies. *J. Appl. Polym. Sci.* **134**, 44380 (2017).
44. M. L. Heuzé *et al.*, Myosin II isoforms play distinct roles in adherens junction biogenesis. *Elife* **8**, e46599 (2019).
45. L. P. Sullivan, D. P. Wallace, J. J. Grantham, Coupling of cell volume and membrane potential changes to fluid secretion in a model of renal cysts. *Kidney Int.* **45**, 1369–1380 (1994).
46. G. A. Tanner, M. R. Maxwell, J. A. McTeer, Fluid transport in a cultured cell model of kidney epithelial cyst enlargement. *J. Am. Soc. Nephrol.* **2**, 1208–1218 (1992).
47. R. Mangoo-Karim *et al.*, Renal epithelial fluid secretion and cyst growth: The role of cyclic AMP. *FASEB J.* **3**, 2629–2632 (1989).
48. M. I. Choudhury *et al.*, Kidney epithelial cells are active mechano-biological fluid pumps. *Nat. Commun.* **13**, 2317 (2022).
49. D. Meder, A. Shevchenko, K. Simons, J. Füllekrug, Gp135/podocalyxin and NHERF-2 participate in the formation of a preapical domain during polarization of MDCK cells. *J. Cell Biol.* **168**, 303–313 (2005).
50. C. B. Collares-Buzato, G. T. A. McEwan, M. A. Jepson, N. L. Simmons, B. H. Hirst, Paracellular barrier and junctional protein distribution depend on basolateral extracellular Ca²⁺ in cultured epithelia. *Biochim. Biophys. Acta* **1222**, 147–158 (1994).
51. W. Choi *et al.*, Remodeling the zonula adherens in response to tension and the role of afadin in this response. *J. Cell Biol.* **213**, 243–260 (2016).
52. K. B. Gagnon, E. Delpire, Sodium transporters in human health and disease. *Front. Physiol.* **11**, 588664 (2021).
53. M. Haas, B. Forbush III, The Na-K-Cl cotransporter of secretory epithelia. *Annu. Rev. Physiol.* **62**, 515–534 (2000).
54. M. F. Schliifka, J. G. Dumortier, D. Pelzer, A. Mukherjee, J.-L. Maître, Inverse blebs operate as hydraulic pumps during mouse blastocyst formation. *Nat. Cell Biol.* **26**, 1669–1677 (2024).
55. F. Huang *et al.*, Studies on expression and function of the TMEM16A calcium-activated chloride channel. *Proc. Natl. Acad. Sci. U.S.A.* **106**, 21413–21418 (2009).
56. G. Shim, I. B. Breinyn, A. Martínez-Calvo, S. Rao, D. J. Cohen, Bioelectric stimulation controls tissue shape and size. *Nat. Commun.* **15**, 2938 (2024).
57. J. E. Lever, Inducers of mammalian cell differentiation stimulate dome formation in a differentiated kidney epithelial cell line (MDCK). *Proc. Natl. Acad. Sci. U.S.A.* **76**, 1323–1327 (1979).
58. J. E. Lever, "Inducers of dome formation in epithelial cell cultures including agents that cause differentiation" in *Tissue Culture of Epithelial Cells*, M. Taub, Ed. (Springer, US, Boston, MA, 1985), pp. 3–22, 10.1007/978-1-4684-4814-6_1.
59. L. Kocgozlu *et al.*, Epithelial cell packing induces distinct modes of cell extrusions. *Curr. Biol.* **26**, 2942–2950 (2016).
60. L. Balasubramanian *et al.*, Dynamic forces shape the survival fate of eliminated cells. *Nat. Phys.* **21**, 269–278 (2025), 10.1038/s41567-024-02716-5.
61. E. A. Slee *et al.*, Benzoyloxycarbonyl-Val-Ala-Asp (OMe) fluoromethylketone (Z-VAD.FMK) inhibits apoptosis by blocking the processing of CPP32. *Biochem. J.* **315**, 21–24 (1996).
62. A. Torres-Sánchez, M. Kerr Winter, G. Salbreux, Tissue hydraulics: Physics of lumen formation and interaction. *Cells Dev.* **168**, 203724 (2021).
63. S. Marbach, L. Bocquet, Osmosis, from molecular insights to large-scale applications. *Chem. Soc. Rev.* **48**, 3102–3144 (2019).
64. O. Kedem, A. Katchalsky, Thermodynamic analysis of the permeability of biological membranes to non-electrolytes. *Biochim. Biophys. Acta* **27**, 229–246 (1958).
65. E. Latorre *et al.*, Active superelasticity in three-dimensional epithelia of controlled shape. *Nature* **563**, 203–208 (2018).
66. H. H. Ussing, K. Eskesen, Mechanism of isotonic water transport in glands. *Acta Physiol. Scand.* **136**, 443–454 (1989).
67. D. D. F. Loo, T. Zeuthen, G. Chandy, E. M. Wright, Cotransport of water by the Na⁺/glucose cotransporter. *Proc. Natl. Acad. Sci. U.S.A.* **93**, 13367–13370 (1996).
68. E. Feraille, A. Sassi, V. Olivier, G. Arnoux, P.-Y. Martin, Renal water transport in health and disease. *Pflügers Arch.* **474**, 841–852 (2022).
69. P. R. Kiela, F. K. Ghishan, Physiology of intestinal absorption and secretion. *Best Pract. Res. Clin. Gastroenterol.* **30**, 145–159 (2016).
70. A. Glentis *et al.*, The emergence of spontaneous coordinated epithelial rotation on cylindrical curved surfaces. *Sci. Adv.* **8**, eabn5406 (2022).
71. Y. Jin *et al.*, Thermally tunable dynamic and static elastic properties of hydrogel due to volumetric phase transition. *Polymers* **12**, 1462 (2020).
72. J. Cappello, V. d'Herbemont, A. Lindner, O. du Roure, Microfluidic in-situ measurement of Poisson's ratio of hydrogels. *Micromachines* **11**, 318 (2020).